

# Intramolecular Energy Transfer Competing with Light-Driven Intermolecular Proton Transfer in an Iron(II)-NHC Complex? A Query into the Role of Photobasic Ligands and MLCT States

Shruthi S. Nair,<sup>†</sup> Oliver A. Bysewski,<sup>†</sup> Niklas Klosterhalfen, Maria Sittig, Andreas Winter, Ulrich S. Schubert,<sup>\*</sup> and Benjamin Dietzek-Ivanšić<sup>\*</sup>



Cite This: *ACS Omega* 2024, 9, 13427–13439



Read Online

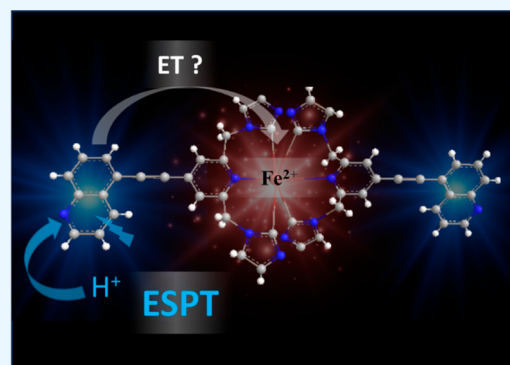
ACCESS |

Metrics & More

Article Recommendations

Supporting Information

**ABSTRACT:** Inorganic photoacids and photobases comprising of photoactive transition metal complexes (TMCs) offer the ability to modulate proton transfer reactions through light irradiation, while utilizing the excellent optical properties of the latter. This provides a powerful tool for precise control over chemical reactions and processes, with implications for both fundamental science and practical applications. In this contribution, we present a novel molecular architecture amending an Fe-NHC complex with a pendant quinoline, as a prototypical photobase, as a representative earth-abundant TMC based inorganic photobase. We characterize the excited-state properties and proton-transfer dynamics using steady-state absorption and emission spectroscopy as well as pump wavelength dependent transient absorption spectroscopy in various protic solvents. The kinetics and thermodynamics of proton transfer in the quinoline moiety are influenced by both the presence of the metal center and the choice of the solvent. Furthermore, we see indications of intramolecular energy transfer from the quinoline to the MLCT state as a limiting factor for panchromatic photobasicity of the complex.



## INTRODUCTION

Photoactive transition metal complexes (TMCs) represent an important area of research owing to their rich and diverse photophysical and photochemical properties.<sup>1,2</sup> The versatility of these complexes has led to a wide range of applications in diverse fields such as photocatalysis, solar-energy harvesting and photodynamic therapy.<sup>3,4</sup> Photoactive TMCs, however, have not only been used as photosensitizers to trigger light-induced electron or energy transfer, either intra- or intermolecularly or at a molecularly functionalized surface. TMC have also been demonstrated to function as, inorganic photoacids/photobases allowing for light-triggered intermolecular proton-transfer reactions.<sup>5–7</sup>

Inorganic photoacids were pioneered in 1976 by Demas and Peterson.<sup>8</sup> Since then, most studies in this area feature Ru(II) complexes with polypyridyl ligands, functionalized with carboxylic<sup>9,10</sup> or amines,<sup>11,12</sup> that show photobasic behavior (or with phenols to yield conceptually complementary photoacids).<sup>13</sup> Recently, Meyer et al. revealed that by modifying the ancillary ligand, the same carboxylic functional group can act as either a photobase or photoacid through control of the localization of the charge-transfer excited states relative to the ligand with conjugated carboxylic-acid groups.<sup>14</sup> Other examples of TMC-based photoacids include complexes of Re(I),<sup>15</sup> Os(II)<sup>16</sup> and Pt(II) centers.<sup>17</sup> Finally, Baitalik et al.

focused on pH-induced processes in multichromophoric heterotrimetallic complex containing Fe(II), Ru(II) and Os(II) polypyridyl moieties.<sup>18</sup> Dawlaty et al. reported metal-orthogonal photobasicity in an iridium complex featuring a pendant quinoline photobase.<sup>19</sup> In this TMC, photobasicity remained unaffected by MLCT excitation but could be triggered by direct excitation of ligand-centered transitions, i.e., direct excitation of the photobasic quinoline group. A similar behavior was observed in a ruthenium-bipyridyl complex with an appended pH-sensitive group.<sup>20</sup>

Our research is directed to Fe(II)-based TMC with photobasic behavior, i.e., expanding the rather well studied photophysics of corresponding Ru(II) systems to Fe(II) complexes as cheap and eco-friendly alternatives to rare and expensive heavy-metal complexes. In this contribution, we report the first attempts to integrate NHC-ligands carrying a quinoline group into Fe(II)- TMCs. In this first generation

**Received:** August 21, 2023  
**Revised:** November 15, 2023  
**Accepted:** November 20, 2023  
**Published:** March 7, 2024



complex, the organic photobase moiety<sup>21–23</sup> is connected via an alkyne linker to the Fe(NHC)<sub>2</sub> structure. This design with its methylene spacer between the pyridine and NHC groups optimizes the octahedral geometry at the metal center, although according to the study by Gros et al., this approach does not significantly improve the MLCT lifetime.<sup>24</sup> Furthermore, the presence of the methylene spacer is meant to limit the electronic influence of the quinoline moiety on the light-absorption of the complex in the spectral range of MLCT transitions; i.e., the quinoline moiety is not interacting with the orbitals of the NHC moiety acting as accepting orbitals upon MLCT excitation. Similar strategies, albeit not with the NHC ligands, have been implemented for Ruthenium complexes.<sup>25,26</sup> Thus, this contribution reports a novel Fe(II)-NHC complex with a photobasic pendant quinoline moiety. Spectroscopically we address the impact of the ligand design on the optical transitions in the TMC and that of the metal coordination on the light-induced changes of the pK<sub>a</sub> value ( $\Delta pK_a$ ) of the quinoline moiety. Furthermore, we evaluate the light-driven excited-state relaxation processes following both direct excitation of the quinoline moiety at higher energies and of the MLCT transitions in the visible spectra range. Thereby, we elucidate the contributions of different excited-state processes to the light-induced dynamics and suggest a model explaining the observed reduced proton-transfer activity of the complex compared to that of the free ligand, even upon direct excitation of quinoline centered transitions.

## EXPERIMENTAL SECTION

**Materials and Instrumentation for Structural Characterization.** Unless stated otherwise, all reactions were carried out using standard Schlenk techniques in a dry nitrogen atmosphere. Dry solvents were purchased from Merck or Across and used as received. Glassware was oven-dried at 110 °C prior to its use. NMR spectra were recorded on a Bruker AVANCE I 300 MHz, AVANCE II 500 MHz or AVANCE III 600 MHz with cryo-probehead instrument in deuterated solvents (Eurisotop) at 25 °C. Chemical shifts are reported in ppm and were referenced using the residual solvent signal. High-resolution electrospray ionization time-of-flight mass spectrometry (ESI-TOF MS) was performed on an ESI-(Q)-TOF-MS MICROTOF II (Bruker Daltonics) mass spectrometer. 2,6-Bis(hydroxymethyl)-4-iodopyridine was synthesized according to literature procedure.<sup>27</sup>

**Synthesis. Synthesis of Compound 1.** 5-Bromoquinoline (10.10 g, 48.54 mmol), tetrakis(triphenylphosphine)palladium(0) (0.98 g, 0.85 mmol), and CuI (0.34 g, 1.81 mmol) were dissolved in a mixture of toluene (120 mL) and triethylamine (10 mL) and purged with nitrogen for 10 min. After the addition of trimethylsilyl acetylene (6.90 g, 70.25 mmol, 10 mL), the reaction mixture was stirred at 50 °C for 18 h. The cooled reaction mixture was filtered over Celite and the solvent was removed under reduced pressure. The crude product was purified by column chromatography [SiO<sub>2</sub>, eluent: hexane:s:ethyl acetate (5:1 → 3:1)] to yield the product as a brown oil (8.40 g, quantitative yield).

<sup>1</sup>H NMR (300 MHz, CDCl<sub>3</sub>):  $\delta$  = 8.94 (dd, 1H, *J* = 4.2 Hz, 1.7 Hz, a-H), 8.62 (ddd, 1H, *J* = 8.5, 1.7, 0.7 Hz, b-H), 8.09 (dt, 1H, *J* = 8.5, 0.7 Hz, c-H), 7.74 (dd, 1H, *J* = 7.2, 1.7 Hz, d-H), 7.64 (dd, 1H, *J* = 8.5, 7.2 Hz, e-H), 7.48 (dd, *J* = 8.5, 4.2 Hz, f-H), 0.32 (s, 9H, TMS) ppm.

<sup>13</sup>C NMR (75 MHz, CDCl<sub>3</sub>):  $\delta$  = 150.03, 148.31, 134.35, 131.08, 130.87, 128.67, 122.43, 121.40, 107.70, 100.39, –0.03 ppm.

**Synthesis of Compound 2.** Compound 1 (4.00 g, 17.75 mmol) and K<sub>2</sub>CO<sub>3</sub> (10.00 g) were suspended in a mixture of THF (50 mL), methanol (20 mL) and water (15 mL). The reaction progress was monitored via TLC; the reaction was stopped after the full consumption of the starting material (2 h). The mixture was poured into water (100 mL) and extracted with dichloromethane (2 × 100 mL). The combined organic phases were dried over Na<sub>2</sub>SO<sub>4</sub> and the solvent was removed under reduced pressure to yield a dark solid (2.70 g, 99%). The crude product was used without further purification.

<sup>1</sup>H NMR (300 MHz, CDCl<sub>3</sub>):  $\delta$  = 8.97 (br s, 1H), 8.69 (d, 1H, *J* = 8.7 Hz), 8.16 (d, 1H, *J* = 8.8 Hz), 7.81 (d, 1H, *J* = 7.2 Hz), 7.70 (t, 1H, *J* = 7.7 Hz), 7.55 (br s, 1H), 3.50 (s, 1H) ppm

<sup>13</sup>C NMR (75 MHz, CDCl<sub>3</sub>):  $\delta$  = 150.73, 147.62, 134.56, 131.57, 130.70, 128.84, 121.87, 120.08, 82.71, 80.39 ppm

**Synthesis of Compound 3.** Compound 2 (0.69 g, 4.53 mmol) and 2,6-bis(hydroxymethyl)-4-iodopyridine (1.00 g, 3.77 mmol), tetrakis(triphenylphosphine)palladium(0) (0.23 g, 0.20 mmol), and CuI (0.08 g, 0.40 mmol) were suspended in a mixture of toluene (40 mL), triethylamine (10 mL), and THF (10 mL). The reaction mixture was stirred at 50 °C for 18 h. After cooling to room temperature, the solid material was filtered off, washed with toluene (2 × 25 mL) and dried to yield the product as a slightly brown solid (1.00 g, 92%).

<sup>1</sup>H NMR (300 MHz, DMSO):  $\delta$  = 8.94 (d, 1H, *J* = 4.0 Hz, a-H), 8.76 (d, 1H, *J* = 8.4 Hz, b-H), 8.13 (d, 1H, *J* = 8.4 Hz, c-H), 8.01 (d, 1H, *J* = 7.2 Hz, d-H), 7.88 (t, 1H, *J* = 7.7 Hz, e-H), 7.75 (dd, *J* = 8.4, 4.1 Hz, f-H), 7.58 (s, 2H, g-H), 5.52 (t, 2H, *J* = 11.6 Hz, O–H), 4.59 (s, 2H, h-H/i-H), 4.57 (s, 2H, CH<sub>2</sub> i-H/h-H) ppm

<sup>13</sup>C NMR (75 MHz, DMSO):  $\delta$  = 161.86, 151.47, 147.36, 133.72, 131.63, 131.09, 130.65, 129.35, 127.82, 122.84, 119.77, 119.31, 92.78, 89.34, 64.96 ppm

HRMS (ESI-TOF, *m/z*): 313.0943, [C<sub>18</sub>H<sub>14</sub>N<sub>2</sub>O<sub>2</sub>+Na]<sup>+</sup> (M<sup>+</sup>) requires 313.0947

**Synthesis of Compound 4.** Compound 3 (0.40 g, 1.38 mmol) was dissolved in anhydrous DMF (10 mL) and the solution cooled to 0 °C. Freshly distilled PBr<sub>3</sub> (0.28 mL, 2.77 mmol) was added dropwise. The suspension was stirred at room temperature for 2 h, and the reaction was quenched by pouring it into an ice-cooled sat. Na<sub>2</sub>CO<sub>3</sub> solution (200 mL). The dark mixture was extracted with CH<sub>2</sub>Cl<sub>2</sub> (3 × 100 mL). The yellow extract was dried over Na<sub>2</sub>SO<sub>4</sub> and the solvent was removed under reduced pressure. The residue was coevaporated with toluene multiple times to remove traces of DMF. The product was yielded as a brown solid (0.40 g, 70%).

<sup>1</sup>H NMR (300 MHz, DMSO):  $\delta$  = 9.16 (br s, 1H, a-H), 9.03 (d, 1H, *J* = 8.3 Hz, b-H), 8.23 (m, 1H, c-H), 8.16 (d, 1H, *J* = 6.9 Hz, d-H), 7.97 (dd, 1H, *J* = 8.2, 7.7 Hz, e-H), 7.91 (dd, *J* = 8.4, 4.4 Hz, f-H), 7.84 (s, 2H, g-H), 4.70 (s, 4H, h-H/i-H) ppm

<sup>13</sup>C NMR (75 MHz, DMSO):  $\delta$  = 162.34, 157.53, 151.48, 147.15, 134.03, 131.92, 131.86, 131.29, 129.49, 127.87, 124.76, 122.88, 118.96, 91.44, 90.72, 69.78 ppm

HRMS (ESI-TOF, *m/z*): 414.9420, [C<sub>18</sub>H<sub>12</sub>Br<sub>2</sub>N<sub>2</sub>+H]<sup>+</sup> (M<sup>+</sup>) requires 414.9440

**Synthesis of Precursor Ligand 5.** Compound 4 (0.200 g, 0.481 mmol) and 1-*n*-butyl-imidazole (0.120 g, 0.961 mmol)

were dissolved in THF (10 mL) and the solution was heated to 50 °C. The reaction was stirred for 4 h at this temperature and then added to a sat. aqueous NaPF<sub>6</sub> solution. The resulting mixture was extracted with a CH<sub>2</sub>Cl<sub>2</sub>/CH<sub>3</sub>CN mixture (100 mL, 9:1 ratio), and the solvents were removed under reduced pressure to yield a yellow-orange oil (0.350 g, 92%).

<sup>1</sup>H NMR (300 MHz, CH<sub>3</sub>CN): δ = 9.00 (dd, 1H, *J* = 3.9, 1.2 Hz, a-H), 8.77 (d, 1H, *J* = 8.4, Hz, b-H), 8.62 (s, 2H, l-H), 8.19 (d, 1H, *J* = 8.4 Hz, c-H), 7.92 (d, 1H, *J* = 6.6 Hz, d-H), 7.80 (dd, 1H, *J* = 7.5, 6.6 Hz, e-H), 7.67 (s, 2H, g-H), 7.65 (dd, *J* = 8.4, 4.2 Hz, f-H), 7.41 (m, 4H, k-H/j-H), 5.61 (s, 4H, h-H/i-H), 4.30 (t, 4H, *J* = 7.3 Hz, N-CH<sub>2</sub>), 1.84 (m, 4H, N-CH<sub>2</sub>-CH<sub>2</sub>), 1.34 (m, 4H, -CH<sub>2</sub>), 0.93 (t, 6H, 7.4 Hz, CH<sub>3</sub>) ppm

<sup>13</sup>C NMR (75 MHz, CH<sub>3</sub>CN): δ = 155.21, 152.91, 149.25, 137.49, 135.02, 134.64, 133.23, 130.46, 129.68, 125.69, 124.74, 123.90, 120.57, 93.28, 92.15, 54.52, 50.88, 32.91, 20.36, 14.35 ppm

HRMS (ESI-TOF, *m/z*): 252.1493, [C<sub>32</sub>H<sub>36</sub>N<sub>6</sub>]<sup>2+</sup> (M<sup>2+</sup>) requires 252.1495

**Synthesis of the Complex.** A mixture of compound 5 (0.450 g, 0.393 mmol) and anhydrous FeBr<sub>2</sub> (0.042g, 0.195 mmol) in anhydrous DMF (10 mL) was cooled to 0 °C. KO<sup>t</sup>Bu (0.89 g, 0.787 mmol) was dissolved in anhydrous DMF (10 mL) and added dropwise to the former solution under vigorous stirring. Thereby, the reaction mixture turned dark blue. After the mixture was stirred for 2 h at room temperature. the reaction mixture was dropped into a sat. NH<sub>4</sub>PF<sub>6</sub> solution (50 mL). It was then extracted with a CH<sub>2</sub>Cl<sub>2</sub>/CH<sub>3</sub>CN mixture (100 mL, 9:1 ratio) and the combined organic phases were washed with water (3 × 300 mL) and dried over Na<sub>2</sub>SO<sub>4</sub>. The solvent was removed under reduced pressure, and the crude product was purified by column chromatography [SiO<sub>2</sub>, eluent: CH<sub>3</sub>CN:H<sub>2</sub>O:KNO<sub>3</sub> (40:4:1)]. The blue fractions were collected and evaporated to afford the product as a dark blue solid (0.02 g, 2%).

<sup>1</sup>H NMR (300 MHz, CH<sub>3</sub>CN): δ = 9.00 (dd, 1H, *J* = 4.3, 1.7 Hz, a-H), 8.69 (d, 1H, *J* = 8.0, Hz, b-H), 8.20 (d, 1H, *J* = 8.4 Hz, c-H), 7.91 (dd, 1H, *J* = 7.3, 1.0 Hz, d-H), 7.82 (dd, 1H, *J* = 8.4, 7.3 Hz, e-H), 7.64 (dd, *J* = 8.4, 4.2 Hz, f-H), 7.52 (br s, 2H, g-H), 7.46 (br s, 2H, j-H/k-H), 7.12 (br s, 2H, k-H/j-H), 5.30 (d, 2H, *J* = 16.02 Hz, h-H/i-H), 4.12 (br s, 2H, i-H/h-H), 2.40 (br s, 2H, N-CH<sub>2</sub>), 1.73 (br s, 2H, N-CH<sub>2</sub>), 1.34 (br s, 2H, N-CH<sub>2</sub>-CH<sub>2</sub>), 0.88 (br s, 2H, N-CH<sub>2</sub>-CH<sub>2</sub>), 0.74 (br s, 2H, -CH<sub>2</sub>), 0.58 (t, 6H, *J* = 7.4 Hz, CH<sub>3</sub>), 0.51 (br s, 2H, -CH<sub>2</sub>) ppm

<sup>13</sup>C NMR (75 MHz, CH<sub>3</sub>CN): δ = 162.37, 152.17, 148.43, 134.11, 132.62, 132.44, 130.77, 129.73, 128.85, 125.95, 123.76, 123.18, 122.87, 119.55, 95.05, 90.94, 54.46, 47.26, 31.97, 20.34, 13.29 ppm

HRMS (ESI-TOF, *m/z*): 530.2496, [C<sub>64</sub>H<sub>68</sub>FeN<sub>12</sub>]<sup>2+</sup> (M<sup>2+</sup>) requires 530.2514

#### Steady-State Absorption and Emission Spectroscopy.

For all spectroscopic measurements, the compounds were dissolved in air-equilibrated solvents of spectrophotometric grade. Steady-state absorption spectra were recorded on a Jasco V-670 spectrophotometer. For measuring the steady-state emission spectra, a FLS980 emission spectrometer (Edinburgh Instruments) with a Xe lamp (ozone-free 450 W xenon bulb) as the excitation source was utilized. Absolute quantum yields were determined from solution samples by using an integrating sphere. The excitation wavelength was set to 300 nm, and the OD of the samples at the excitation

wavelength was kept in the range of 0.05 to 0.1. All steady-state spectroscopic measurements were done in 1 cm quartz cuvettes.

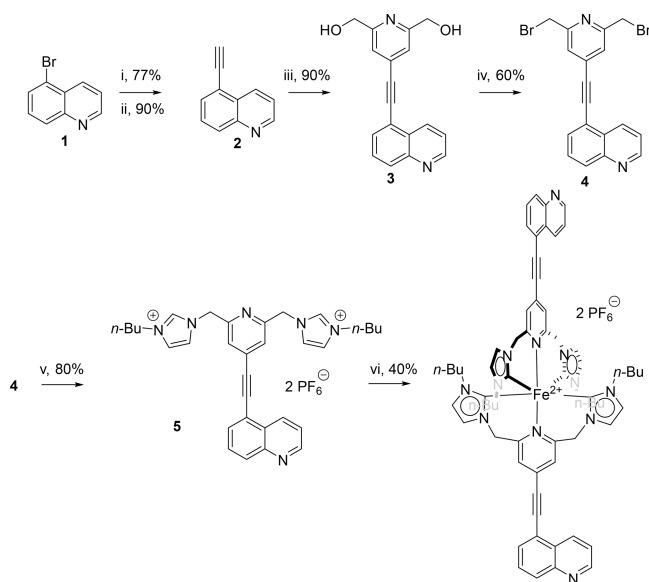
**Transient Absorption Spectroscopy.** The ultrafast transient absorption (TA) experiments were performed using a custom-built setup similar to the one described in detail elsewhere.<sup>28,29</sup> A Ti-Sapphire (Astrella, Coherent, USA) regenerative amplifier, which produces 800 nm, 85 fs pulses (laser power 5 mJ, with a pulse-to-pulse repetition rate of 1 kHz), was employed. The output of the laser was then divided by a beam splitter. The first part was focused into a rotating CaF<sub>2</sub> crystal to generate a broadband white light super-continuum beam covering the range of 300 to 700 nm. This broadband pulse was subsequently split into two parts, which were used as the reference and probe pulse, respectively. The second fraction of the amplifier output was directed to an optical parametric amplifier (TOPAS prime, Light conversion, Lithuania) to generate pump pulses, tunable across the UV–vis–NIR spectral range (in this study, we used it to generate pump pulses centered at 340 and 650 nm). A mechanical chopper periodically blocked every alternate pump pulse, reducing the repetition rate to 500 Hz. A Berek compensator and a polarizer were used to set the relative polarization between pump and probe pulses to the magic angle of 54.7°. The probe pulse was focused into a quartz cuvette with a path length of 1 mm by a concave mirror with a focal length of 500 mm focal length. The spectra of probe and reference pulses were acquired by a 150 mm focal length Czerny–Turner spectrograph (SP2150, Princeton Instruments) equipped with two CCD arrays (Pascher Instruments AB, Sweden). Since strong contributions of coherent artifact signals were observed,<sup>30</sup> this temporal pulse overlap range of ±150 fs was removed from the data analysis procedure. The fs-TA data was analyzed using the KIMOPACK tool.<sup>31</sup> Prior to global lifetime analysis, the data were numerically corrected for the chirp of the white-light probe. The power of pump-pulse used was in the range of 0.4 to 0.8 mW, and OD of sample at the excitation wavelength was in the range of 0.3 to 0.5.

**Time-Resolved Emission Studies.** The fluorescence lifetimes were obtained by streak-camera measurements. A frequency doubled Ti-Sapphire Laser (Tsunami, Newport Spectra-Physics GmbH) was used as the light source to generate the 390 nm excitation pulses. The pulse-to-pulse repetition rate of the laser was reduced to 4 kHz by a pulse selector (Model 3980, Newport Spectra-Physics GmbH). The emission was recorded using a CHROMEX 250IS spectrograph and a Hamamatsu HPD-TA streak-camera. The power of the pump-pulse used was in the range of 0.2 mW, and the OD of the sample at the excitation wavelength was in the range of 0.05 to 0.1.

## RESULTS AND DISCUSSION

**Synthesis and Characterization.** The synthesis of the ligand precursor was accomplished via an established synthetic route (Scheme 1). The starting material *–2,6-bis(hydroxymethyl)–4-iodopyridine–*is accessible via a procedure published elsewhere. The quinoline building block 2 was synthesized by a Sonogashira-type cross-coupling reaction starting from 5-bromoquinoline and the subsequent deprotection of intermediate 1 under basic conditions. The iodo compound and acetylene derivative 2 were cross-coupled under typical Sonogashira reaction conditions. Notably, one could also perform the cross-coupling reaction using ester

### Scheme 1. Schematic Representation of the Synthesis of the Target Fe(II) Complex<sup>a</sup>



<sup>a</sup>Where i stands for Pd(PPh<sub>3</sub>)<sub>4</sub>, CuI, TMS-acetylene, toluene, NEt<sub>3</sub>, 50 °C; ii for K<sub>2</sub>CO<sub>3</sub>, MeOH, room temp.; iii for (PPh<sub>3</sub>)<sub>4</sub>, CuI, TMS-acetylene, toluene, NEt<sub>3</sub>, 50 °C; iv for PBr<sub>3</sub>, DMF, room temp.; v for *n*-Bu imidazole, THF, room temp.; vi for KO<sup>t</sup>Bu, FeBr<sub>2</sub>, DMF, 0 °C.

instead of alcohol, but when alcohol is used, product **3** precipitates during the reaction and can readily be filtered off. Purification of **3** was realized by simply washing the crude product with toluene. The hydroxy groups of **3** were subsequently transformed by treatment with freshly distilled PBr<sub>3</sub>. For the synthesis of **4**, the usage of fresh PBr<sub>3</sub> is of importance since traces of POBr<sub>3</sub> lead to undesired side reactions. DMF is used as a solvent for this reaction step, as is **3** insoluble in dichloromethane. *n*-Butyl-imidazole and **4** are reacted in THF to afford, after anion exchange, the precursor ligand **5**. The latter was reacted in a one-pot reaction with potassium *tert*-butoxide and anhydrous FeBr<sub>2</sub> in DMF. The resulting Fe(II) complex was finally purified via a salt-assisted column chromatography on silica (eluent: acetonitrile, water, saturated aqueous potassium nitrate; 40:4:1 ratio) and isolated as a blue viscous oil.

The <sup>1</sup>H NMR spectrum of the metal complex (Figure S12) no longer shows the proton signal of the NHC precursor (i.e., singlet at 8.61 ppm). The signal of the bridging CH<sub>2</sub>-groups split from a singlet at 5.42 ppm to a doublet at 5.30 ppm and a broad signal at 4.12 ppm. This feature is characteristic for TMCs with such methylene bridges due to the adopted helix-type structure.<sup>32–34</sup> These protons become diastereotopic upon complexation, and they lose their freedom of rotation. The signals of the *n*-butyl group protons, except that of the terminal CH<sub>3</sub> group, also show signal broadening as well as splitting into pairs of signals. They are more shielded in the complex than in the ligand precursor and thus are shifted accordingly in the NMR spectrum. The signal of the pyridine proton is also more shielded, and the signal becomes broadened. It is shifted from 7.67 to 7.18 ppm. However, the protons of the imidazolium moiety in the complex are less shielded than those in the precursor but also broadened (shift from 7.41 to 7.62 ppm), whereas the protons of the quinoline moiety do not show any difference in shielding and the

chemical shifts of these protons in the complex remain the same as in the precursor.

The signal broadening can be rationalized by the frequency of flipping of the helical structure. As the methylene bridge is rather flexible, a structural change from one conformer to another is enabled. This process is known to be dependent on the temperature of the solvent environment. If the NMR spectra are recorded in DMSO instead of CH<sub>3</sub>CN, the broad signal of the CH<sub>2</sub>-bridge at 4.12 ppm turned into a sharp doublet. We conducted temperature-dependent <sup>1</sup>H NMR studies in DMSO to determine the frequency of the conformer change. However, coalescence of the signals could not be detected when the mixture was heated up until 80 °C (Figure S14). The frequency of inversion is thus slower than the time scale of the NMR experiment.

The <sup>13</sup>C NMR spectrum of the complex shows all of the expected signals. Due to the aforementioned conformational changes, the signals of the NHC carbon as well as the imidazolium carbons, the methylene bridging carbons, and the *n*-butyl groups all exhibit signal broadening. The signal of the NHC carbon is shifted from 137.5 to 162.4 ppm. Such small shifting is indicative of a weak  $\sigma$ -donating effect from the carbene. Furthermore, a <sup>1</sup>H-coupled <sup>13</sup>C NMR experiment was performed in order to gauge the  $\sigma$ -donating properties of the ligand. This very simple method, which utilizes the readily available precursor salt instead of the metal complex, enables a combined measurement of the  $\sigma$ -donating,  $\pi$ -back bonding and steric contributions.<sup>35</sup> The thus determined <sup>1</sup>J coupling constant is 217.6 Hz. This value suggests that the ligand is a weaker  $\sigma$ -donor compared to other known ligands; this finding is in line with the conclusion drawn from the <sup>13</sup>C NMR experiment.

This effect is traced to the introduction of the quinoline group, which is linked to the metal complex via an alkyne moiety. The parent complex without any chromophore on the coordinated pyridine ring was studied before by Gros et al.<sup>24</sup> That pink complex had a signal of the NHC carbon at 191.4 ppm in the <sup>13</sup>C NMR. Assuming that the differences in electronic and steric contributions from the alkyl substituents are marginal (i.e., methyl vs *n*-butyl), the difference of ca. 29 ppm is due to the different electron donation of the NHC ligand. Presumably, electron density is spread out over the entire ligand framework including the conjugated quinoline chromophore.

**Steady-State Absorption.** Figure 1 shows the extinction coefficient spectra of the ligand precursor (**5**) and complex in the CH<sub>3</sub>CN solution. The two intense bands in the UV region in both molecules are attributed to  $\pi\pi^*$  transitions within the quinoline moiety. The corresponding electronic states are denoted as <sup>1</sup>L<sub>a</sub> and <sup>1</sup>L<sub>b</sub> according to the Platt notation for cata-condensed hydrocarbons.<sup>36</sup> <sup>1</sup>L<sub>b</sub> refers to bond-centered excess charge density in the excited state and has a sharp absorption line. Whereas, <sup>1</sup>L<sub>a</sub> refers to atom-centered excess charge density and is responsible for the photobasic behavior of quinoline, as it shifts electron density toward quinoline's heteroatom.<sup>21</sup> Furthermore, the  $\pi\pi^*$  band in the complex appears red-shifted by ca. 10 nm, i.e., 859 cm<sup>-1</sup>, with respect to that of the ligand. In addition to the intense quinoline bands, the complex also contains a broad visible MLCT band with a maximum at 650 nm. In comparison to the parent complex by Gros et al., the MLCT transition in the complex investigated here appears red-shifted.<sup>24</sup> This suggests that the ethynyl-

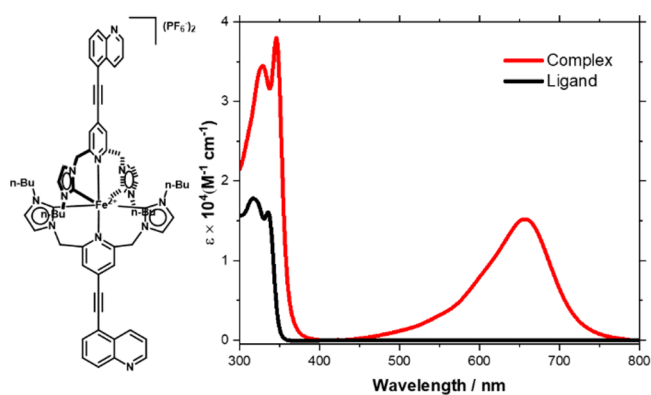


**Figure 1.** Chemical structure and extinction coefficient of the investigated complex and ligand in acetonitrile.

quinolin-5-yl chromophore is stabilizing the acceptor orbitals involved in the  $^1\text{MLCT}$  transition.

**Estimation of  $pK_a$  Values—pH Titration.** UV/vis titration in aqueous buffered solutions of varying pH values enables an estimation of the ground-state acidity constant,  $pK_a$ . Following this approach, the  $pK_a$  values of the ligand precursor and complex were estimated to be 3.7 and 4.6 in aqueous medium, respectively (Figures S19 and S20). At  $\text{pH} > pK_a$ , the respectively unprotonated species dominate the absorption spectra, which in this case resemble the absorption spectra recorded in  $\text{CH}_3\text{CN}$ , as a nonprotonating solvent (Figure 1). Upon lowering the pH ( $\text{pH} < pK_a$ ), the absorption band of  $^1\text{L}_b$  at 340 nm remains spectrally unchanged while its intensity is reduced. On the other hand, the  $^1\text{L}_a$  transition shifts to 360 nm with a concurrent increase in intensity. The emission of the unprotonated species is centered at 370 nm, both for **5** and the complex; whereas, the emission of the protonated species is observed at 460 nm. In addition to the spectral shift, the emission intensity also increases upon protonation. Using Förster's cycle analysis and considering optical excitation of the quinoline moiety at 300 nm (see SI for more details), the  $pK_a^*$  of **5** and the complex are determined as 11 and 12, respectively. Hence, both ligand precursor and complex experience a UV light-induced increase of their respective basicity by 7 orders of magnitude, indicating that the inherent

photobasicity of the quinoline is indeed retained upon integration into the complex structure. The absorption and emission spectra in both **5** and complex are dominated by the electronic transitions within the quinoline moiety (see Figure S21, where the absorption and emission properties of the ligand are compared to that of 5-ethynylquinoline and the ligand of the parent complex<sup>24</sup>). The electronic transitions corresponding to the NHC-pyridyl group lies deep in the UV and remain invariant to pH changes in the pH range from 1 to 8 and in  $\text{CH}_3\text{CN}$ , and is nonemissive at RT.

**Protonation in Various Solvents.** To understand the protonation behavior further, studies were carried out in various protic solvents. The solvents were chosen such that they allow for studying unprotonated, protonated, and partially protonated quinoline moieties in the excited state. To this end, we employed methanol ( $\text{MeOH}$ ,  $pK_a = 15.5$ ),<sup>37</sup> trifluoroethanol (TFE,  $pK_a = 12.4$ )<sup>38</sup> and hexafluoroisopropanol (HFiP,  $pK_a = 9.3$ ).<sup>39</sup> It is important to note that the  $pK_a$  values of these alcohols were reported with respect to water; the  $pK_a$  and  $pK_a^*$  of the ligand and complex were determined in an aqueous medium as well. By using a common scale with respect to water, we aim to facilitate a comparison of  $pK_a$  values and dynamics among the different solvents, providing a more convenient and straightforward interpretation of the results. In the ground state, all three solvents are not acidic enough to protonate the quinoline (i.e.,  $pK_a$  of solvent  $> pK_a$  of complex/**5**). Hence, the ground-state absorption spectra of **5** and the complex in all three solvents reflect the absorption properties of the unprotonated quinoline. Nonetheless, the MLCT band in the complex appears to be blue-shifted in HFiP (most polar) compared to MeOH (least polar). On the other hand, the MLCT band is red-shifted upon reducing the pH value of the solution from 10 to 1 (Figure S22). H-bonding effects are likely responsible for this observation.

Upon optical excitation of the quinoline moieties, the  $pK_a^*$  increases in both ligand precursor and complex, and solvents whose  $pK_a < pK_a^*$  of **5**/complex can protonate the quinoline in the excited state. Such excited-state protonation shifts not only the absorption but also the emission bands of the quinoline derivatives. Considering **5** in MeOH, the emission band is centered at 380 nm, corresponding to the unprotonated quinoline. In HFiP, the emission is red-shifted

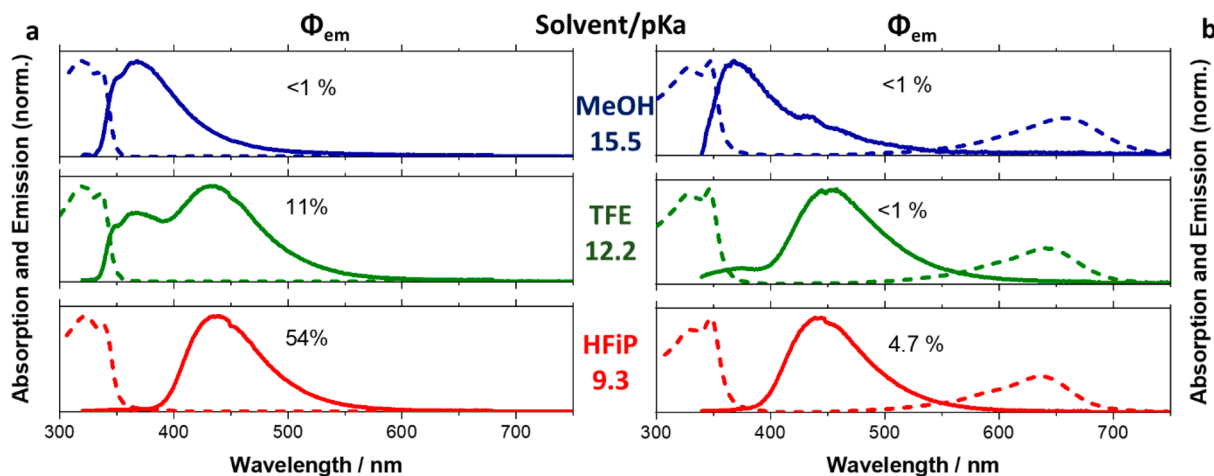


**Figure 2.** Normalized absorption (dashed line) and emission (solid line) spectra of (a) ligand precursor **5** and (b) complex upon excitation at 300 nm in protic solvents MeOH, TFE, and HFiP with corresponding  $pK_a$  of solvent. The respective quantum yield of emission ( $\Phi_{em}$ ) upon excitation at 300 nm is indicated in the respective panel.

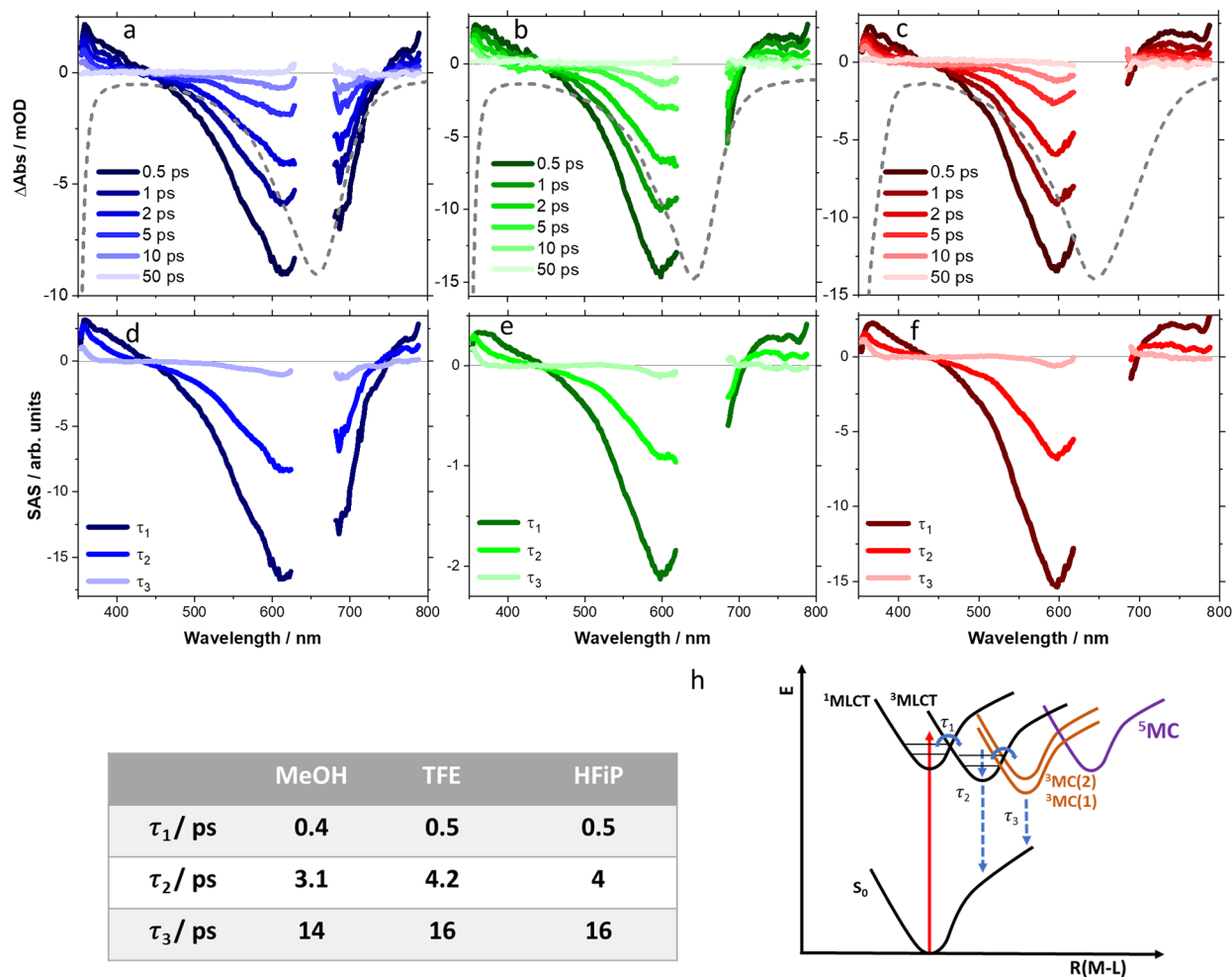


**Figure 3.** (a–c) TA spectra and (d–f) species associated spectra of the complex in different solvents in MeOH (column 1), TFE (column 2), and HFiP (column 3), respectively, following excitation at 650 nm. The region from 630 to 690 nm is disregarded due to excessive pump scattering. The dashed line in TAS shows the inverted steady state spectra. (h) Schematic model for the observed dynamics along with the table showing the corresponding time constants for sequential fit. Note that the dashed line in (h) showing  $\tau_2$  and  $\tau_3$  indicates nonradiative relaxation.

to 440 nm, thus confirming the protonation of **5**. In TFE, there are two bands, centered at 380 and 430 nm, suggesting partial protonation of **5** in TFE. For MeOH and HFiP as solvents, the emission spectra of the complex resemble those of the ligand with emission at 380 and 445 nm. Also, in TFE the emission spectrum indicates partial protonation of the complex. However, in TFE a different degree of protonation is observed comparing **5** and the complex, i.e., the ratio of the emission of the protonated and unprotonated species at the respective emission maxima is 0.72 in **5** and 0.17 in the complex.

Not only the spectral characteristics but also the quantum yield of emission ( $\Phi_{em}$ ) strongly depends on the extent of protonation (see Figure 2).  $\Phi_{em}$  is highest for the fully protonated ligand precursor, i.e., in HFiP (54%), followed by TFE (11%). The unprotonated form in MeOH is poorly emissive (<1%). The  $\Phi_{em}$  of the complex is drastically reduced compared to that of the ligand. This trend in  $\Phi_{em}$  is mirrored in the emission lifetimes, which for protonated **5** in HFiP was estimated to 6 ns, while for **5** in the other solvents or the complexes no time-resolved emission signal could be detected with our streak camera setup (see Figure S23). We hypothesize that the predominant pathway leading to emission quenching is an intramolecular energy transfer from the quinoline to the Fe(NHC)<sub>2</sub> moiety, which routes the considerable spectral

overlap of the emission of quinoline (donor) and the absorption spectra of the MLCT (acceptor). We will return to this hypothesis in the context of the pump-wavelength-dependent transient-absorption data (*vide infra*).

**Transient Absorption Studies.** To study the photoinduced excited-state relaxation, transient absorption (TA) studies were performed in MeOH, TFE and HFiP. In these studies, we excited both the complex and **5** at 340 nm, populating the quinoline excited states and activating the photobasic properties. In addition, the complex was excited at 650 nm to compare the dynamics induced by MLCT excitation to the dynamics observed upon excitation of the quinoline.

$\lambda_{ex} = 650$  nm – **Excited-State Relaxation of the Complex upon MLCT Excitation.** Upon excitation at 650 nm, i.e., excitation of the <sup>1</sup>MLCT transition, the TA spectra (TAS, Figure 3a–c) show ground-state bleach (GSB) between 450 to 700 nm and excited-state absorption (ESA) bands in the blue region below 450 nm and in the red region above 700 nm. The TA spectral features are very similar in all three solvents. Global analysis of the TA data using a sequential kinetic scheme reveals three characteristic decay constants, with  $\tau_1 \approx 0.4$  to 0.5 ps,  $\tau_2 \approx 3$  to 4 ps, and  $\tau_3 \approx 14$  to 16 ps (Figure 3). The corresponding species-associated spectra (SAS) are shown in Figure 3d–f. The spectral changes associated with  $\tau_1$

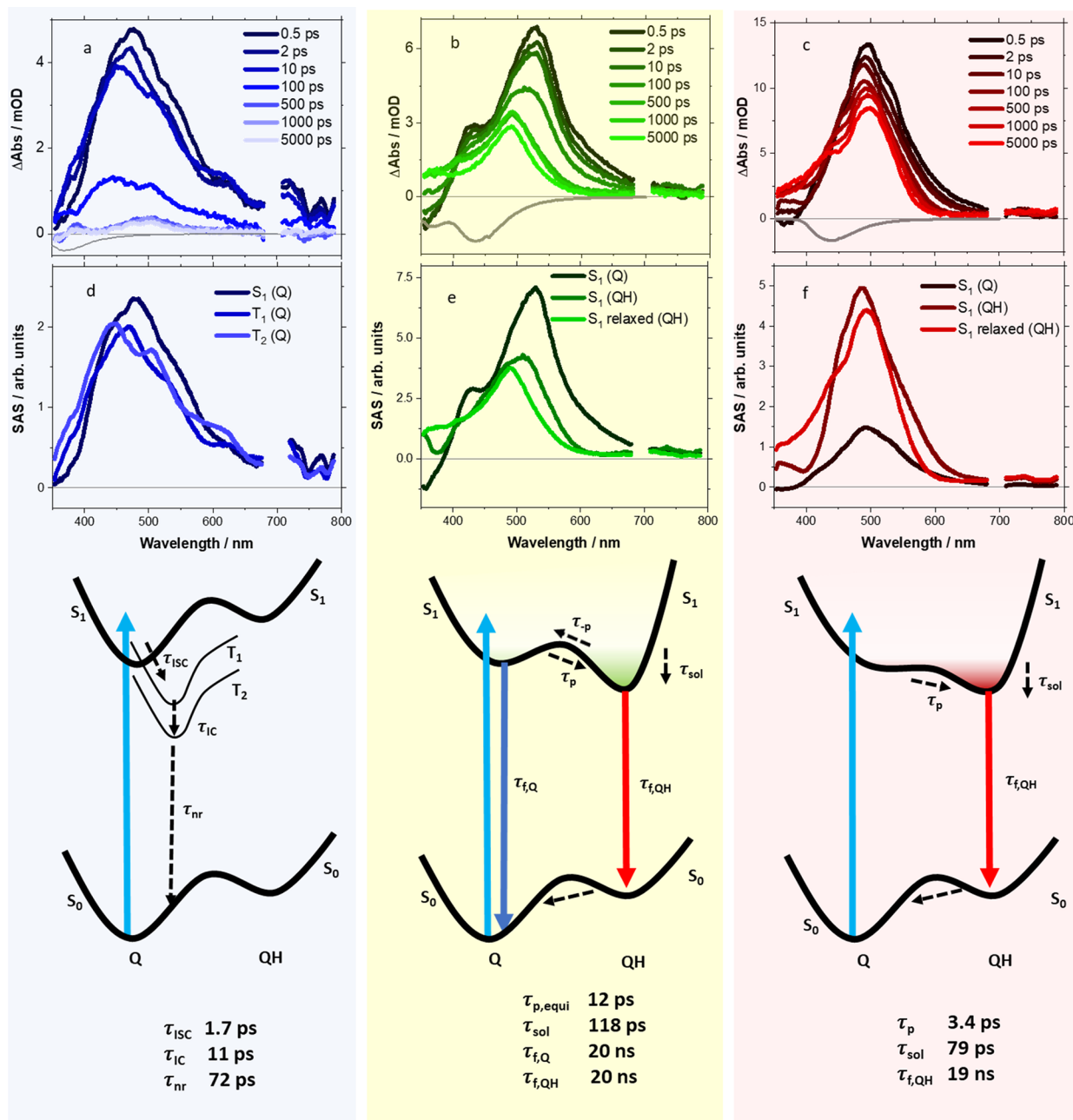


**Figure 4.** (a–c) TA spectra and (d–f) species associated spectra of ligand precursor **5** in different solvents MeOH (column 1), TFE (column 2), and HFIP (column 3), respectively, following excitation at 340 nm. The gray line in TAS shows the inverted steady state emission. The signal around 690 nm is removed due to second order diffraction artifact caused by the scattering of the pump (340 nm) at the grating of the spectrometer. Note: SAS shows estimated amplitudes associated with the concentration profile of each species involved, irrespective of the total number of decay components associated with various processes. Schematic model used for fitting the data along with the corresponding time constants is shown for each solvent (row 3). The potential energy curve is plotted along the proton transfer gradient. Q denotes unprotonated quinoline, and QH denotes protonated quinoline. The dashed black lines in the schematic show nonradiative transitions. Note that the activation energy barrier for proton transfer is different in each case.

describe the decrease in ESA centered at the blue and red regions. These spectral features are quite typical of MLCT states of Fe(II) complexes (where the ESA at  $\sim 370$  nm and broad featureless above 700 nm are signatures of reduced pyridyl ligand<sup>40,41</sup>). The ISC from <sup>1</sup>MLCT to <sup>3</sup>MLCT in Fe(II)-polypyridyl complexes was experimentally determined to be of the order of 30 fs through ultrafast X-ray emission studies.<sup>42</sup> The subpicosecond process in our case represented by  $\tau_1$  may be too slow to be associated with ISC and instead is probably some charge localization within MLCT.<sup>43</sup> The

process associated with  $\tau_2$  describes the reduction in amplitude of the red-ESA as well as narrowing of the blue-ESA. This might be attributed to vibrational relaxation within the <sup>3</sup>MLCT and concurrently populating the <sup>3</sup>MC as shown by Gros et al., that the methylene bridge between the pyridyl group and NHC increases the flexibility of the Fe–N bond and the <sup>3</sup>MC is easily populated through Fe–N stretching.<sup>24</sup> The spectral changes associated with  $\tau_1$  and  $\tau_2$  account for most changes associated with the GSB signal suggesting that the major contribution to GSB recovery occurs by direct relaxation from

the  $^1/3\text{MLCT}$  to the ground state. The decay of species associated with  $\tau_3$  has almost no ESA in the red-region and has very sharp and narrow blue-ESA and negligible GSB accounting for the remaining ground state recovery. With the major signature of MLCT being absent, it may be predominantly associated with the nonradiative decay of the remaining small fraction of molecules via the  $^3\text{MC}$  state back to the ground state. The absence of slow ground-state recovery (i.e., in the range of few hundreds of picoseconds or few nanoseconds), it can be assumed that the  $^5\text{MC}$  is destabilized and hence not populated.<sup>44</sup> The dynamics are summarized in the relaxation scheme in Figure 3h.

$\lambda_{\text{ex}} = 340 \text{ nm}$  – *Excited-State Relaxation in the Ligand upon Excitation of the Quinoline Moiety*. Understanding the excited-state dynamics observed in quinoline is rather complex, and at this point, it is necessary to discuss the nature of the underlying electronic states and their sensitivity to the solvent environment. In addition to the  $^1\pi\pi^*$  states (i.e.,  $^1\text{L}_{\text{a/b}}$ ), also  $n\pi^*$  states need to be considered, which arise from the presence of nonbonding electrons. While  $^1n\pi^*$  lies relatively deep in the UV region, the  $^3n\pi^*$  state is approximately degenerate with the  $^1\pi\pi^*$ .<sup>22</sup> Heteroaromatic systems, such as quinoline, tend to show a polarity-induced inversion of excited states; i.e., with increasing polarity or H-bonding, the  $n\pi^*$  gets destabilized, while the  $\pi\pi^*$  becomes stabilized. The strong dependence of the close-lying  $^1\pi\pi^*$  and  $^3n\pi^*$  states on the solvent environment leads to a significant change in the intersystem crossing rate. In this context, the El-Sayed rules state that the rate of ISC is relatively large if the radiation-less transition involves a change of orbital type.<sup>45</sup> Hence, it was found that ISC in quinolines, in solvents of low polarity, is very fast and the probability for nonradiative relaxation is higher. However, in more polar solvents, upon proton addition or increased H-bonding, ISC is prevented. This finding is ascribed either to a loss of the nonbonding character of the lowest excited state or to a significant rise in  $n\pi^*$  energy.<sup>46</sup> Hence, the solvent is expected to have a major impact on the excited-state dynamics; the following discussion is divided into three sections corresponding to each solvent.

*MeOH*. Excitation of the quinoline band at 340 nm populates  $^1\pi\pi^*$  states (lowest state denoted as  $S_1$ ). The initial TA spectrum is composed of broad ESA signals spanning the range between 350 and 800 nm with a maximum at 450 nm. Within the first 10 ps, a sharpening of the ESA band is observed. Subsequently, the differential absorption signal decays within 100 ps without further spectral evolution (Figure 4a). A weak residual signal remains visible even at delay times longer than 100 ps. Global analysis of the TA data using a sequential kinetic scheme reveals three characteristic time constants (i.e.,  $\tau_{\text{ISC}} = 1.7 \text{ ps}$ ,  $\tau_{\text{IC}} = 11 \text{ ps}$ , and  $\tau_{\text{nr}} = 72 \text{ ps}$ ; see Figure 4d). Figure S24 shows the TA spectra of 5-ethylquinoline upon excitation of the quinoline band at 320 nm, and it is spectrally similar to that observed in the case of ligand in MeOH, suggesting that the dynamics is mainly dominated by that of quinoline. The steady-state emission of **5** in MeOH (*vide supra*) indicates the absence of excited-state protonation and low quantum yields of emission. Consistently, the TA studies indicate an overall short excited-state lifetime. Together, the results point to efficient ISC in MeOH. The shortest characteristic time constant  $\tau_{\text{ISC}}$  may thus be assigned to ISC populating the  $^3n\pi^*$  state (denoted as  $T_2$ ).<sup>19</sup>  $\tau_{\text{IC}}$ , which is associated with spectral sharpening and shifting of the ESA, can be assigned to the  $T_2 \rightarrow T_1$  internal conversion (IC)

leading to population of a (short-lived)  $^3\pi\pi^*$  state (denoted as  $T_1$ ). The ESA band centered at 440 nm is correspondingly associated with excited-state absorption within the triplet manifold.  $\tau_{\text{nr}}$  accounts for the majority of the excited-state decay and can be ascribed to the nonradiative relaxation to the ground state. The fact that we can detect (weak) steady-state emission upon excitation at the UV suggests the possibility of a weak radiative relaxation channel. The fact that we can detect (weak) steady-state emission upon excitation at the UV suggests the possibility of a weak radiative relaxation channel. The residual TA signal that decays on a slower time scale maybe related to this radiative channel. Currently, it is not clear whether this very minor decay pathway is associated with residual fluorescence or phosphorescence from the  $^1\pi\pi^*/^3\pi\pi^*$ , respectively. However, the feasibility of phosphorescence from  $^3\pi\pi^*$  appears more likely as it seems not likely that the emission from the singlet state would effectively compete with the fast and efficient ISC process. Additionally, the observed spectral shift in the excited-state absorption (ESA) bands, transitioning from an initial 440 to 500 nm for the residual long-lived signal, indicates significant alterations in the excited-state nature.

*HFiP*. The initial TA spectrum (recorded at  $\Delta t = 0.5 \text{ ps}$ ) in HFiP is mainly composed of a strong ESA band spanning between 400 and 700 nm with an ESA maximum at 500 nm. In addition to this band, a minor negative differential absorption signal is observed at early delay times and probe wavelengths around 380 nm. This feature spectrally matches the emission spectrum of the unprotonated species and hence is associated with stimulated emission (SE). The SE signal diminishes within ca. 3 ps and grows into a positive ESA signal. During this delay time range, the broad ESA centered at 500 nm decreases in intensity. Furthermore, a diplike feature appears at 440 nm, which resembles the stimulated emission of the protonated quinoline (*vide supra*). This feature becomes more pronounced with increasing delay times. Afterward, the differential absorption signal decays without further spectral changes. The decay of the photoinduced signals exceeds the experimentally accessible delay time window. The transient absorption signals can be quantitatively described by three characteristic time constants (i.e.,  $\tau_{\text{p}} = 3.4 \text{ ps}$ ,  $\tau_{\text{sol}} = 79 \text{ ps}$ , and  $\tau_{\text{fQH}} = 19 \text{ ns}$ ), whereas the latter only presents a coarse estimate due to the limited range of pump–probe delays accessible in our experimental setup (see Figure 4f). The UV excitation initially populates the  $^1\pi\pi^*$  ( $S_1$ ) of the unprotonated species (unlike in MeOH, in more polar solvents such as HFiP, the  $n\pi^*$  are higher lying and ultrafast ISC into the  $^3n\pi^*$  is prevented). The spectral changes associated with  $\tau_{\text{p}}$  describe the diminishing SE signal corresponding to the fluorescence of the unprotonated species (at 390 nm) and the onset of SE (at 440 nm) due to the fluorescence of the protonated species corresponding to the singlet states of the respective species. Eventually, the protonated species decays back radiatively as fluorescence (described by  $\tau_{\text{fQH}}$ ) to the protonated ground state. Hence,  $\tau_{\text{p}}$  might be associated with the protonation time. The spectral change associated with  $\tau_{\text{sol}} = 70 \text{ ps}$  seems to be related to structural relaxation within protonated  $S_1$ . The corresponding time constant seems too large to be associated with vibrational cooling, rendering it more plausible that global intra- and intermolecular reorganization of the system after proton transfer, i.e., including solvent reorganization around the protonated base and the acid anion. It may be related to “anion escape” from the local solvent cage involving the

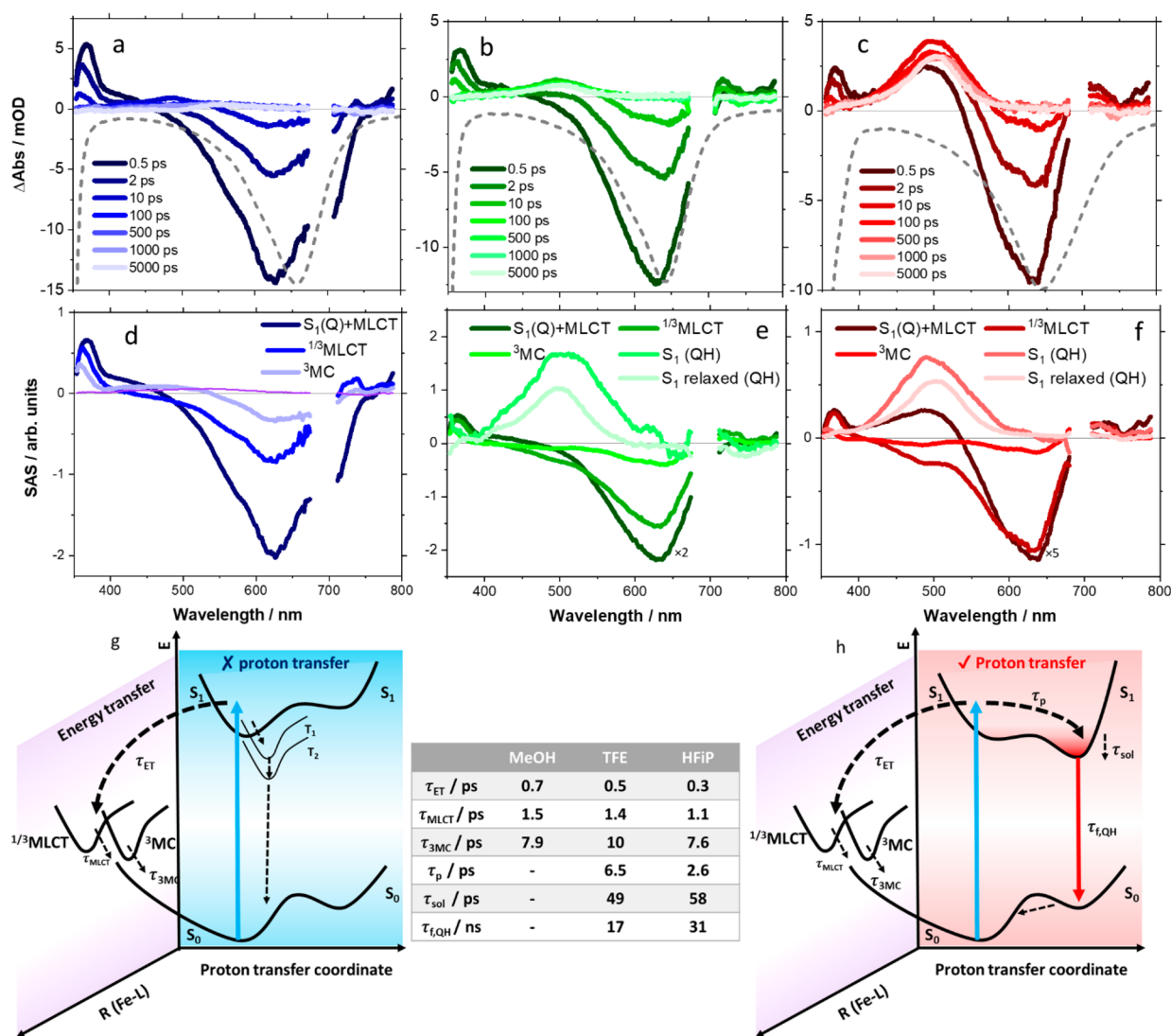


**Figure 5.** (a–c) TA spectra and (d–f) species associated spectra in different solvents MeOH (row 1), TFE (row 2), and HFIP (row 3) of the complex following excitation at 340 nm. The gray dashed line in TAS shows the inverted steady state absorption spectra. Schematic model used for fitting the data along with the corresponding time constants are shown for each solvent (row 3). (g) Schematic model of dynamics in MeOH, fit with sequential decay fit, and probable mechanism for decay including the emissive channel. (h) Schematic model used for target analysis and fitting the data in TFE/HFiP with the table showing corresponding time constants. The signal around 690 nm is removed due to second order diffraction artifact caused by the scattering of the pump (340 nm) at the grating of the spectrometer. Please note that the SAS of HFIP and TFE involving the MLCT branch are multiplied by a scaling factor of 5 and 2, respectively.

separation of protonated photobase and the alkoxide anion.<sup>47</sup> Eventually, the protonated species decays back radiatively (described by  $\tau_{f,QH}$ ) to the protonated ground state; however, the protonated ground state is not observed as intermediate because it deprotonates faster than it is formed from the protonated excited state.

**TFE.** The TA spectrum at 0.5 ps reveals broad, structured ESA with a maximum at 540 nm and a shoulder at 420 nm and negative signal below 400 nm (see Figure 4b). The negative signal (centered at 380 nm) spectrally coincides with the steady-state emission of the unprotonated species and is assigned to SE of the unprotonated species. Compared to the spectrally similar SE observed in HFIP, it is almost five times higher in magnitude in the case of TFE. The ESA band is structured probably due to overlapping SE signal originating from the protonated species (as it overlaps with the steady state emission). Unlike in HFIP, where the dip in ESA

appeared after  $\sim 20$  ps, in TFE contributions of such spectral features are visible in the data almost immediately after photoexcitation, i.e., already at a delay time of 0.5 ps. This points to at least one subensemble of photobases being present which are strongly H-bonded to the solvent already in the ground-state. The linear structure of TFE in comparison to HFIP is likely the reason for stronger hydrogen bonding in the former.

The spectral features evolve drastically with an increase in delay times. The negative SE signal from the unprotonated species diminishes and grows into a positive ESA signal within ca. 20 ps. The ESA maximum blue-shifts from 540 to 500 nm over the span of  $\sim 100$  ps and becomes spectrally narrower. The dip in ESA due to SE from protonated species also undergoes a blue-shift and becomes less pronounced. The TA spectrum recorded at very long delay times, i.e., at  $\Delta t = 5000$  ps, looks very similar to that of HFIP (i.e., the protonated

form) at  $\Delta t = 5000$  ps, indicating (at least partial protonation observed also in TFE). Nonetheless, the dynamics in TFE appear to be kinetically more complicated than the other two solvents, in line with the dual emission observed for TFE, which indicates partial protonation in TFE since the excited state  $pK_a^*$  is very close to the  $pK_a$  of TFE. This means that a fraction of excited-state population remains unprotonated while the rest is protonated, suggesting a dynamic quasi-equilibrium existing between the two forms.<sup>7</sup> Hence proton transfer is reversible and is a crucial factor to consider when fitting and modeling the excited state dynamics. A simple parallel or sequential model is, therefore, not enough to adequately describe the complex mechanism. Instead, we used a target model within global analysis as illustrated in Figure S25, described by the kinetic rate equations described in the figure. The rate equations were formulated for each of the states ( $S_1(Q)$ ,  $S_1(QH)$ ,  $S_{1,relaxed}(QH)$ , and  $S_0(QH)$ ) participating in the relaxation scheme, outlining how their populations influence one another with the help of 5 time constants ( $\tau_{f,Q}$ ,  $\tau_p$ ,  $\tau_{-p}$ ,  $\tau_{sol}$ , and  $\tau_{f,QH}$ ). Here,  $\tau_p$  describes protonation while  $\tau_{-p}$  describes the reverse proton transfer or deprotonation.  $\tau_{f,Q}$  and  $\tau_{f,QH}$  refer to the radiative lifetime of the unprotonated and protonated forms, respectively.  $\tau_{sol}$  describes the global intra- and intermolecular reorganization of the system after proton transfer, i.e., similar to the case described in HFiP above. However, it is important to note that, in practice, it may not be possible to distinguish between the forward and backward proton transfer reactions. Numerically, we might observe two distinct time constants, but in reality, we would perceive only a combined rate,  $\tau_{p,eq} = (k_p + k_{-p}) = (1/\tau_p + 1/\tau_{-p})$ . These rate equations were subsequently solved using the KiMoPack software package.<sup>31</sup> This leads to our final model yielding time constants as  $\tau_{f,Q} = 20$  ns,  $\tau_{p,eq} = 12$  ps,  $\tau_{sol} = 118$  ps, and  $\tau_{f,QH} = 20$  ns, as given in Figure 4. Please refer to the fitting procedure described in Supporting Information and Figure S29 for more details.

$\lambda_{ex} = 340$  nm – Excited-State Relaxation of the Complex upon Excitation of the Quinoline Moiety. 340 nm excitation of the complex in MeOH (Figure 5a) leads to an early time TA spectrum with significant contributions from GSB at 650 nm (overlapping with the ground-state absorption spectra of the MLCT state) and ESA; a comparably strong ESA band at 360 nm is observed together with a comparatively weak band at 700 nm. These signals decay within less than 20 ps without any significant residual TA signal discernible. Quantitative analysis of the data using a three-component sequential relaxation scheme yields the characteristic time constants  $\tau_{ET} = 0.7$  ps,  $\tau_{MLCT} = 1.5$  ps, and  $\tau_{3MC} = 7.9$  ps. These characteristic time constants and the overall spectral features are very reminiscent of the data observed for exciting the <sup>1</sup>MLCT transition of the complex at 650 nm. The fact that excitation of the quinoline moiety at 340 nm leads to MLCT/MC dynamics characteristic for the Fe(II) core of the complex indicates very rapid, i.e., within the range of our experimental time resolution, energy transfer from the pendant quinoline to the Fe(NHC)<sub>2</sub> moiety. An additional weak-long-lived decay is also present and likely is related to the weak emission observed in the steady state absorption spectra, but cannot be resolved in the TA data for fitting. We have indicated a probable model (Figure 5g) with the major channel deactivating via the MLCT states and the other probable channel derived from the model for **5** in MeOH to account for the observed steady-state emission). Also, when using TFE (Figure 5b) or HFiP as solvent (Figure 5c), the

initial TAS reveal features of MLCT excitation, i.e., GSB signal at 650 nm, and ESA bands at 360 and 700 nm. In addition to this, there is a third ESA region at 500 nm (stronger in HFiP compared to TFE). While the TA features corresponding to MLCT excitation decay within 20 ps, the ESA band at 500 nm grows in intensity until 20 ps and then decays slowly. The band at 500 nm, which is distinct from the spectral features observed upon direct <sup>1</sup>MLCT excitation, may be assigned to protonated species since it is absent in MeOH while present in TFE and HFiP. Such an assignment is in line with the steady-state spectra, which indicate excited-state protonation in TFE/HFiP, while this is absent in MeOH. This assignment is further corroborated by the TA data of the fully protonated complex shown in Figure S26. If the complex is protonated in the ground state by an acidic buffer solution with pH 1 and subsequently excited at 340 nm, the TAS shows a prominent ESA at 500 nm, which is similar to the spectral signal seen in Figure 5.

The SAS associated with  $\tau_{ET}$  (340 nm excitation) is very similar to the SAS of  $\tau_1$  (650 nm excitation) and points to the possibility that they may represent the same process, i.e., there is the possibility of non-negligible absorption of the Fe(NHC)<sub>2</sub> moiety at 340 nm and the potential formation of the MLCT state through the rapid deactivation of higher excited states within the directly excited Fe(NHC)<sub>2</sub> moiety. However, the apparent absence of GSB when exciting the quinoline in already protonated species in the ground state points more in the direction of the energy transfer mechanism (Figure S26). Our hypothesis for the apparent absence of energy transfer when it is protonated in the ground state is that it could be due to different angular orientation of the donor and acceptor molecules in the ground and excited states. The quinoline's orientation relative to the Fe-NHC core can get distorted from planarity when protonated in the ground state, and therefore the energy transfer is hindered.<sup>48,49</sup> Protonation of the quinoline may alter the energy states of the electronic system in a manner that diminishes electronic coupling, ultimately resulting in the absence of energy transfer. Furthermore, the ESA band at 500 nm corresponding to the protonated species exhibits a considerably longer lifetime compared to the MLCT bleach. This observation suggests that the excited state of the protonated ligand is no longer coupled to the MLCT state and there is no energy transfer from the former to the latter. Instead, energy transfer occurs exclusively right after optical excitation from the quinoline moiety to the MLCT state- after  $\tau_{ET}$ , a fraction of molecules resides in the MLCT state, while the rest stays in the excited state of the quinoline moiety.

## CONCLUSION

We have synthesized and characterized a novel Fe(II)-NHC complex that contains a pendent quinoline moiety. The quinoline retained its photobasicity in both ligand and complex showing an increase in  $pK_a^*$  by  $\Delta pK_a^* = 7$  units upon photoexcitation. The protonation behavior in various protic solvents (MeOH, TFE, and HFiP) was studied by using steady-state absorption and emission measurements. The excited state dynamics in these solvents were probed using fs-TA studies upon excitation of the quinoline band at 340 nm and the MLCT state at 650 nm. Both steady state and TA studies indicate the absence of protonation in MeOH with efficient ISC limiting the excited state lifetime. In TFE, there was partial protonation with the existence of a dynamic equilibrium between the two species, while in HFiP, there was

full protonation with proton transfer estimated to occur within a few tens of picoseconds in both ligand and complex. In addition, we see indications for intramolecular energy transfer from the quinoline (donor) to the MLCT (acceptor) independent of the proton-transfer process in the complex due to spectral overlap of donor-emission and acceptor-absorption, which may be a limiting factor for the panchromatic photobasicity of the complex.

## ■ ASSOCIATED CONTENT

### SI Supporting Information

The Supporting Information is available free of charge at <https://pubs.acs.org/doi/10.1021/acsomega.3c06196>.

Details on the synthesis and characterization of the ligand and complex, pH titration and Förster cycle analysis for determination of  $pK_a$  and  $pK_a^*$ , respectively, comparison of absorption and emission properties of **5**, ligand of parent complex, ethynyl quinoline, streak camera emission data for ligand in HFiP, TA spectra of 5-ethynylquinoline, TA spectra for complex in pH 1 upon excitation of quinoline band, TA-raw data, and kinetics with fits (PDF)

## ■ AUTHOR INFORMATION

### Corresponding Authors

**Ulrich S. Schubert** – Laboratory of Organic and Macromolecular Chemistry (IOMC), Friedrich Schiller University Jena, 07743 Jena, Germany; Center for Energy and Environmental Chemistry Jena (CEEC Jena), Friedrich Schiller University Jena, Jena 07743, Germany; [orcid.org/0000-0003-4978-4670](https://orcid.org/0000-0003-4978-4670); Email: [ulrich.schubert@uni-jena.de](mailto:ulrich.schubert@uni-jena.de)

**Benjamin Dietzek-Ivanšić** – Department Functional Interfaces, Leibniz Institute of Photonic Technology (Leibniz-IPHT), 07745 Jena, Germany; Institute of Physical Chemistry, Friedrich-Schiller University Jena, 07743 Jena, Germany; [orcid.org/0000-0002-2842-3537](https://orcid.org/0000-0002-2842-3537); Email: [benjamin.dietzek@leibniz-ipht.de](mailto:benjamin.dietzek@leibniz-ipht.de)

### Authors

**Shruthi S. Nair** – Department Functional Interfaces, Leibniz Institute of Photonic Technology (Leibniz-IPHT), 07745 Jena, Germany; Institute of Physical Chemistry, Friedrich-Schiller University Jena, 07743 Jena, Germany

**Oliver A. Bysewski** – Laboratory of Organic and Macromolecular Chemistry (IOMC), Friedrich Schiller University Jena, 07743 Jena, Germany; Center for Energy and Environmental Chemistry Jena (CEEC Jena), Friedrich Schiller University Jena, Jena 07743, Germany; Present Address: Agilent Technologies Deutschland GmbH, Hewlett-Packard-Str. 8, 76337 Waldbronn, Germany

**Niklas Klosterhalfen** – Department Functional Interfaces, Leibniz Institute of Photonic Technology (Leibniz-IPHT), 07745 Jena, Germany; Institute of Physical Chemistry, Friedrich-Schiller University Jena, 07743 Jena, Germany

**Maria Sittig** – Department Functional Interfaces, Leibniz Institute of Photonic Technology (Leibniz-IPHT), 07745 Jena, Germany; Institute of Physical Chemistry, Friedrich-Schiller University Jena, 07743 Jena, Germany; Present Address: Bayer Weimar GmbH and Co. KG, Döbereiner Str. 20, 99427 Weimar, Germany

**Andreas Winter** – Laboratory of Organic and Macromolecular Chemistry (IOMC), Friedrich Schiller University Jena, 07743 Jena, Germany; Center for Energy and Environmental Chemistry Jena (CEEC Jena), Friedrich Schiller University Jena, Jena 07743, Germany; [orcid.org/0000-0003-0757-8721](https://orcid.org/0000-0003-0757-8721)

Complete contact information is available at: <https://pubs.acs.org/doi/10.1021/acsomega.3c06196>

### Author Contributions

<sup>†</sup>S.S.N. and O.A.B. contributed equally. The manuscript was written through contributions of all authors. All authors have given approval to the final version of the manuscript.

### Notes

The authors declare no competing financial interest.

## ■ ACKNOWLEDGMENTS

We would like to thank the Deutsche Forschungsgemeinschaft [Priority Program SPP 2102 “Light-controlled reactivity of metal complexes” (projects DI1517/31-1 and SCHU1229/62-1)] for financially supporting our work.

## ■ ABBREVIATIONS

TMC, transition metal complexes; MLCT, metal to ligand charge transfer; MC, metal centric; NHC, N-heterocyclic carbene; Q, quinoline; QH, quinolinium; MeOH, methanol; TFE, trifluoroethanol; HFiP, hexafluoro isopropanol; GSB, ground state bleach; SE, stimulated emission; ESA, excited state absorption; ISC, intersystem crossing; IC, internal conversion

## ■ REFERENCES

- (1) Campagna, S.; Puntoriero, F.; Nastasi, F.; Bergamini, G.; Balzani, V. Photochemistry and photophysics of coordination compounds: ruthenium. *Photochemistry photophysics of coordination compounds I* **2007**, *280*, 117–214.
- (2) Akulov, K.; Simkovitch, R.; Erez, Y.; Gepshtein, R.; Schwartz, T.; Huppert, D. Acid effect on photobase properties of curcumin. *J. Phys. Chem. A* **2014**, *118* (13), 2470–2479.
- (3) Zhang, T.; Lin, W. Metal–organic frameworks for artificial photosynthesis and photocatalysis. *Chem. Soc. Rev.* **2014**, *43* (16), 5982–5993.
- (4) Monro, S.; Colon, K. L.; Yin, H.; Roque, J., III; Konda, P.; Gujar, S.; Thummel, R. P.; Lilge, L.; Cameron, C. G.; McFarland, S. A. Transition metal complexes and photodynamic therapy from a tumor-centered approach: challenges, opportunities, and highlights from the development of TLD1433. *Chem. Rev.* **2019**, *119* (2), 797–828.
- (5) Gianneschi, N. C.; Masar, M. S.; Mirkin, C. A. Development of a coordination chemistry-based approach for functional supramolecular structures. *Accounts of chemical research* **2005**, *38* (11), 825–837.
- (6) Kramarz, K.; Norton, J. Slow proton-transfer reactions in organometallic and bioinorganic chemistry. *Prog. Inorg. Chem.* **1994**, *42*, 1–65.
- (7) Bysewski, O.; Sittig, M.; Winter, A.; Dietzek-Ivanšić, B.; Schubert, U. S. Photobasic transition-metal complexes. *Coord. Chem. Rev.* **2024**, *498*, No. 215441.
- (8) Peterson, S. H.; Demas, J. Excited state acid-base reactions of transition metal complexes: dicyanobis (2, 2′-bipyridine) ruthenium (III) in aqueous acid. *J. Am. Chem. Soc.* **1976**, *98* (24), 7880–7881.
- (9) Nazeeruddin, M. K.; Kalyanasundaram, K. Acid-base behavior in the ground and excited states of ruthenium (II) complexes containing tetraamines or dicarboxybipyridines as protonatable ligands. *Inorg. Chem.* **1989**, *28* (23), 4251–4259.

- (10) Higgins, B.; DeGraff, B.; Demas, J. Luminescent transition metal complexes as sensors: structural effects on pH response. *Inorganic chemistry* **2005**, *44* (19), 6662–6669.
- (11) Cargill Thompson, A. M. W.; Smailes, M. C. C.; Jeffery, J. C.; Ward, M. D. Ruthenium tris-(bipyridyl) complexes with pendant protonatable and deprotonatable moieties: pH sensitivity of electronic spectral and luminescence properties. *J. Chem. Soc., Dalton Trans.* **1997**, *1997* (5), 737–744.
- (12) Kirsch-De Mesmaeker, A.; Jacquet, L.; Nasielski, J. Ruthenium (II) complexes of 1, 4, 5, 8-tetraazaphenanthrene (TAP) and 2, 2'-bipyridine (bpy). Ground-and excited-state basicities of Ru<sup>2+</sup> (bpy) *n* (TAP) 3-*n* (*n* = 0, 1, 2): their luminescence quenching by organic buffers. *Inorg. Chem.* **1988**, *27* (24), 4451–4458.
- (13) Giordano, P. J.; Bock, C. R.; Wrighton, M. S. Excited state proton transfer of ruthenium (II) complexes of 4, 7-dihydroxy-1, 10-phenanthroline. Increased acidity in the excited state. *J. Am. Chem. Soc.* **1978**, *100* (22), 6960–6965.
- (14) O'Donnell, R. M.; Sampaio, R. N.; Li, G.; Johansson, P. G.; Ward, C. L.; Meyer, G. J. Photoacidic and photobasic behavior of transition metal compounds with carboxylic acid group (s). *J. Am. Chem. Soc.* **2016**, *138* (11), 3891–3903.
- (15) Leasure, R.; Sacksteder, L.; Nesselrodt, D.; Reitz, G.; Demas, J.; DeGraff, B. Excited-state acid-base chemistry of (α-dimine) cyanotricarbonylrhenium (I) complexes. *Inorg. Chem.* **1991**, *30* (19), 3722–3728.
- (16) Browne, W. R.; O'Connor, C. M.; Hughes, H. P.; Hage, R.; Walter, O.; Doering, M.; Gallagher, J. F.; Vos, J. G. Ruthenium (II) and osmium (II) polypyridyl complexes of an asymmetric pyrazinyl- and pyridinyl-containing 1, 2, 4-triazole based ligand. Connectivity and physical properties of mononuclear complexes. *J. Chem. Soc., Dalton Trans.* **2002**, No. 21, 4048–4054.
- (17) Cummings, S. D.; Eisenberg, R. Acid-base behavior of the ground and excited states of platinum (II) complexes of quinoxaline-2, 3-dithiolate. *Inorg. Chem.* **1995**, *34* (13), 3396–3403.
- (18) Maity, D.; Mardanya, S.; Karmakar, S.; Baitalik, S. pH-Induced processes in wire-like multichromophoric homo- and heterotrimetallic complexes of Fe (II), Ru (II), and Os (II). *Dalton transactions* **2015**, *44* (21), 10048–10059.
- (19) Demianets, I.; Hunt, J. R.; Dawlaty, J. M.; Williams, T. J. Optical p K a Control in a Bifunctional Iridium Complex. *Organometallics* **2019**, *38* (2), 200–204.
- (20) Guardigli, M.; Flamigni, L.; Barigelletti, F.; Richards, C. S.; Ward, M. D. Proton Sensitivity of Luminescent [M (bpy) 2 (AB)] 2+ Complexes and Their Monomethylated Counterparts [M (bpy) 2 (ABMe)] 3+ Where AB Is an Asymmetric Quaterpyridine with a Pendant Bipyridyl Site [M= RuII, OsII]. *J. Phys. Chem.* **1996**, *100* (25), 10620–10628.
- (21) Driscoll, E. W.; Hunt, J. R.; Dawlaty, J. M. Photobasicity in quinolines: origin and tunability via the substituents' Hammett parameters. *J. Phys. Chem. Lett.* **2016**, *7* (11), 2093–2099.
- (22) Driscoll, E. W.; Hunt, J. R.; Dawlaty, J. M. Proton capture dynamics in quinoline photobases: substituent effect and involvement of triplet states. *J. Phys. Chem. A* **2017**, *121* (38), 7099–7107.
- (23) Hunt, J. R.; Dawlaty, J. M. Photodriven deprotonation of alcohols by a quinoline photobase. *J. Phys. Chem. A* **2018**, *122* (40), 7931–7940.
- (24) Darari, M.; Francés-Monerris, A.; Marekha, B.; Doudouh, A.; Wenger, E.; Monari, A.; Haacke, S.; Gros, P. C. Towards Iron(II) Complexes with Octahedral Geometry: Synthesis, Structure and Photophysical Properties. *Molecules* **2020**, *25* (24), 5991–6011.
- (25) Weinheimer, C.; Choi, Y.; Caldwell, T.; Gresham, P.; Olmsted, J., III Effect of a steric spacer on chromophoric interactions of ruthenium complexes containing covalently bound anthracene. *Journal of Photochemistry Photobiology A: Chemistry* **1994**, *78* (2), 119–126.
- (26) McClenaghan, N. D.; Leydet, Y.; Maubert, B.; Indelli, M. T.; Campagna, S. Excited-state equilibration: a process leading to long-lived metal-to-ligand charge transfer luminescence in supramolecular systems. *Coordination chemistry reviews* **2005**, *249* (13–14), 1336–1350.
- (27) Godt, A.; Qi, M.; Hülsmann, M. Synthesis and Hydrolysis of 4-Chloro-PyMTA and 4-Iodo-PyMTA Esters and Their Oxidative Degradation with Cu(I/II) and Oxygen. *Synthesis* **2016**, *48* (21), 3773–3784.
- (28) Kübel, J.; Schroot, R.; Wächtler, M.; Schubert, U. S.; Dietzek, B.; Jäger, M. Photoredox-active dyads based on a Ru (II) photosensitizer equipped with electron donor or acceptor polymer chains: a spectroscopic study of light-induced processes toward efficient charge separation. *J. Phys. Chem. C* **2015**, *119* (9), 4742–4751.
- (29) Siebert, R.; Akimov, D.; Schmitt, M.; Winter, A.; Schubert, U. S.; Dietzek, B.; Popp, J. Spectroscopic Investigation of the Ultrafast Photoinduced Dynamics in π-Conjugated Terpyridines. *ChemPhysChem* **2009**, *10* (6), 910–919.
- (30) Dietzek, B.; Pascher, T.; Sundström, V.; Yartsev, A. Appearance of coherent artifact signals in femtosecond transient absorption spectroscopy in dependence on detector design. *Laser Physics Letters* **2007**, *4* (1), 38.
- (31) Müller, C.; Pascher, T.; Eriksson, A.; Chabera, P.; Uhlig, J. KiMoPack: A python Package for Kinetic Modeling of the Chemical Mechanism. *J. Phys. Chem. A* **2022**, *126* (25), 4087–4099.
- (32) Lee, C.-S.; Sabiah, S.; Wang, J.-C.; Hwang, W.-S.; Lin, I. J. B. Water-Induced Changes of Photoluminescence of a Pincer-Type N-Heterocyclic Carbene Platinum(II) Complex. *Organometallics* **2010**, *29* (2), 286–289.
- (33) Dinda, J.; Adhikary, S. D.; Roymahapatra, G.; Nakka, K. K.; Santra, M. K. Synthesis, structure, electrochemistry and cytotoxicity studies of Ru(II) and Pt(II)–N-heterocyclic carbene complexes of CNC-pincer ligand. *Inorg. Chim. Acta* **2014**, *413*, 23–31.
- (34) Zhang, X.; Wright, A. M.; DeYonker, N. J.; Hollis, T. K.; Hammer, N. I.; Webster, C. E.; Valente, E. J. Synthesis, Air Stability, Photobleaching, and DFT Modeling of Blue Light Emitting Platinum CCC-N-Heterocyclic Carbene Pincer Complexes. *Organometallics* **2012**, *31* (5), 1664–1672.
- (35) Meng, G.; Kakalis, L.; Nolan, S. P.; Szostak, M. A simple 1H NMR method for determining the σ-donor properties of N-heterocyclic carbenes. *Tetrahedron Lett.* **2019**, *60* (4), 378–381.
- (36) Platt, J. R. Classification of spectra of cata-condensed hydrocarbons. *J. Chem. Phys.* **1949**, *17* (5), 484–495.
- (37) Ballinger, P.; Long, F. Acid Ionization Constants of Alcohols. II. Acidities of Some Substituted Methanols and Related Compounds. *J. Am. Chem. Soc.* **1960**, *82* (4), 795–798.
- (38) Donghi, D.; Beringhelli, T.; D'Alfonso, G.; Mondini, M. NMR Investigation of the Dihydrogen-Bonding and Proton-Transfer Equilibria between the Hydrido Carbonyl Anion [HRe2 (CO) 9]– and Fluorinated Alcohols. *Chemistry—A European Journal* **2006**, *12* (4), 1016–1025.
- (39) Middleton, W.; Lindsey, R. Hydrogen bonding in fluoro alcohols. *J. Am. Chem. Soc.* **1964**, *86* (22), 4948–4952.
- (40) Liu, Y.; Harlang, T.; Canton, S. E.; Chábera, P.; Suárez-Alcántara, K.; Fleckhaus, A.; Vithanage, D. A.; Göransson, E.; Corani, A.; Lomoth, R.; et al. Towards longer-lived metal-to-ligand charge transfer states of iron (II) complexes: an N-heterocyclic carbene approach. *Chem. Commun.* **2013**, *49* (57), 6412–6414.
- (41) Kaufhold, S.; Wärnmark, K. Design and synthesis of photoactive iron n-heterocyclic carbene complexes. *Catalysts* **2020**, *10* (1), 132.
- (42) Zhang, K.; Ash, R.; Girolami, G. S.; Vura-Weis, J. Tracking the metal-centered triplet in photoinduced spin crossover of Fe (phen) 32+ with tabletop femtosecond M-edge X-ray absorption near-edge structure spectroscopy. *J. Am. Chem. Soc.* **2019**, *141* (43), 17180–17188.
- (43) Paulus, B. C.; Nielsen, K. C.; Tichnell, C. R.; Carey, M. C.; McCusker, J. K. A Modular Approach to light capture and synthetic tuning of the excited-state properties of Fe (II)-based chromophores. *J. Am. Chem. Soc.* **2021**, *143* (21), 8086–8098.

- (44) Gütlich, P. Spin crossover, LIESST, and NIESST-Fascinating electronic games in iron complexes. *Mol. Cryst. Liq. Cryst.* **1997**, *305* (1), 17–40.
- (45) Baba, M. Intersystem Crossing in the  $1n\pi^*$  and  $1\pi\pi^*$  States. *J. Phys. Chem. A* **2011**, *115* (34), 9514–9519.
- (46) Anton, M. F.; Moomaw, W. R. Luminescence and hydrogen bonding in quinoline and isoquinoline. *J. Chem. Phys.* **1977**, *66* (5), 1808–1818.
- (47) Sittig, M.; Tom, J. C.; Elter, J. K.; Schacher, F. H.; Dietzek, B. Quinoline Photobasicity: Investigation within Water-Soluble Light-Responsive Copolymers. *Chem.—Eur. J.* **2021**, *27* (3), 1072–1079.
- (48) Broquier, M.; Soorkia, S.; Dedonder-Lardeux, C.; Juvet, C.; Theulé, P.; Grégoire, G. Twisted intramolecular charge transfer in protonated amino pyridine. *J. Phys. Chem. A* **2016**, *120* (21), 3797–3809.
- (49) Giribabu, L.; Ashok Kumar, A.; Neeraja, V.; Maiya, B. G. Orientation dependence of energy transfer in an anthracene–porphyrin donor–acceptor system. *Angew. Chem., Int. Ed.* **2001**, *40* (19), 3621–3624.